Bioactive Materials 40 (2024) 306–317

Contents lists available at ScienceDirect

Bioactive Materials

journal homepage: www.keaipublishing.com/en/journals/bioactive-materials

Bioceramic-mediated chondrocyte hypertrophy promotes calcified cartilage formation for rabbit osteochondral defect repair

Rachel H. Koh [a], Junhee Kim [a], Jeong-Uk Kim [a], Seunghyun L. Kim [b], Arun Kumar Rajendran [a], Seunghun S. Lee [c], Heesoo Lee [a], Joo Hyun Kim [d,e], Ji Hoon Jeong [d,e], Yongsung Hwang [d,e], Jong Woo Bae [f,**], Nathaniel S. Hwang [a,b,g,*]

[a] School of Chemical and Biological Engineering, Institute of Chemical Processes, Seoul National University, Seoul, 08826, South Korea
[b] Interdisciplinary Program in Bioengineering, Seoul National University, Seoul, 08826, South Korea
[c] Department of Biomedical Engineering, Dongguk University, Seoul, 10326, South Korea
[d] Soonchunhyang Institute of Medi-bio Science (SIMS), Soonchunhyang University, Cheonan, 31151, South Korea
[e] Department of Integrated Biomedical Science, Soonchunhyang University, Asan, 31538, South Korea
[f] Department of Orthopaedic Surgery, Konkuk University Chungju Hospital, Konkuk University School of Medicine, Chungju, 27376, South Korea
[g] BioMAX Institute, Seoul National University, Seoul, 08826, South Korea

ARTICLE INFO

Keywords:
Bioceramic
Whitlockite
Bilayer scaffold
Chondrocyte hypertrophy
Osteochondral defect repair

ABSTRACT

Osteochondral tissue is a highly specialized and complex tissue composed of articular cartilage and subchondral bone that are separated by a calcified cartilage interface. Multilayered or gradient scaffolds, often in conjunction with stem cells and growth factors, have been developed to mimic the respective layers for osteochondral defect repair. In this study, we designed a hyaline cartilage-hypertrophic cartilage bilayer graft (RGD/RGDW) with chondrocytes. Previously, we demonstrated that RGD peptide-modified chondroitin sulfate cryogel (RGD group) is chondro-conductive and capable of hyaline cartilage formation. Here, we incorporated whitlockite (WH), a Mg^{2+}-containing calcium phosphate, into RGD cryogel (RGDW group) to induce chondrocyte hypertrophy and form collagen X-rich hypertrophic cartilage. This is the first study to use WH to produce hypertrophic cartilage. Chondrocytes-laden RGDW cryogel exhibited significantly upregulated expression of hypertrophy markers *in vitro* and formed ectopic hypertrophic cartilage *in vivo*, which mineralized into calcified cartilage in bone microenvironment. Subsequently, RGD cryogel and RGDW cryogel were combined into bilayer (RGD/RGDW group) and implanted into rabbit osteochondral defect, where RGD layer supports hyaline cartilage regeneration and bioceramic-containing RGDW layer promotes calcified cartilage formation. While the RGD group (monolayer) formed hyaline-like neotissue that extends into the subchondral bone, the RGD/RGDW group (bilayer) regenerated hyaline cartilage tissue confined to its respective layer and promoted osseointegration for integrative defect repair.

1. Introduction

Chondral lesions often span the entire length of the cartilage as full-thickness cartilage defect, or even extend to the underlying subchondral bone as osteochondral defect. If not properly treated, such defects can disrupt normal joint mechanics, function and homeostasis and potentially progress to degenerative arthritis. Since articular cartilage inherently lacks self-repair capacity [1], chondral lesions have limited capacity for spontaneous healing and require external intervention to repair injured tissues. Cell-based surgical approaches such as bone marrow stimulation via microfracture and autologous chondrocyte implantation are used for smaller, early-stage lesions, while auto/allograft transplantation or total knee replacement is required for more severe conditions (i.e. Grade III-IV).

Given the insufficient supply of auto/allografts, tissue engineered cartilage graft is a promising solution for full-thickness and

Peer review under responsibility of KeAi Communications Co., Ltd.
* Corresponding author. School of Chemical and Biological Engineering, Institute of Chemical Processes, Seoul National University, Seoul, South Korea.
** Corresponding author. Department of Orthopaedic Surgery, Konkuk University Chungju Hospital, Konkuk University School of Medicine, Chungju, South Korea.
E-mail addresses: bonedoctor@naver.com (J.W. Bae), nshwang@snu.ac.kr (N.S. Hwang).

https://doi.org/10.1016/j.bioactmat.2024.06.018
Received 15 February 2024; Received in revised form 24 May 2024; Accepted 10 June 2024

osteochondral defect repair. In the past two decades, researchers have developed multilayered and gradient scaffolds using bioactive factors to mimic the anatomical stratified structure of the osteochondral tissue. Chondro-conductive and osteo-inductive biomaterials and bioactive factors were spatially arranged in their respective layers or in concentration gradients. Cartilage extracellular matrix (ECM) components, such as cartilage decellularized matrix [2], hyaluronic acid (HA) [3], type II collagen [4], and sulfated glycosaminoglycan, constituted the cartilaginous phase to provide a chondro-conductive microenvironment. Bioceramics, such as conventional calcium phosphates hydroxyapatite (HAp) [5,6] and beta tricalcium phosphate (β-TCP) [7], are strong osteogenic inducers [8] that were commonly incorporated in the bone portion of composite scaffolds. Recent studies have demonstrated augmented osteochondral defect repair using ion-doped bioceramics [9–11]. Since most studies employed mesenchymal stem cells (MSC) as the cell source, chondrogenic and osteogenic growth factors were used in combination with biomaterials to facilitate MSC differentiation [12]. Research efforts in osteochondral regeneration have primarily focused on engineering hyaline cartilage-bone grafts to recapitulate the major bulks of osteochondral tissue.

Recently, increased attention has been paid to the importance of the calcified cartilage layer that lies between the articular cartilage and subchondral bone. Calcified cartilage is a thin layer of highly mineralized cartilage that contains less type II collagen and aggrecan than hyaline cartilage [13]. This layer plays important structural and functional roles as the osteochondral interface. The interfacial tissue of intermediate matrix stiffness bridges the gap between two mechanically dissimilar tissues and plays a critical role in load transfer during joint motion [14]. Tidemark, an undulating line between the hyaline and calcified cartilage, also provides stress buffer effects that prevent mechanical failure [15]. Moreover, the calcified cartilage helps maintain articular cartilage and subchondral bone as independent physiological environments. The dense mineralized matrix of calcified cartilage acts as a physical barrier between avascular, unmineralized hyaline cartilage and vascularized, mineralized subchondral bone, preventing vascular ingrowth to the cartilage compartment [16]. By acting as a mechanical buffer and compartmentalizing the articular cartilage and underlying bone, the calcified cartilage interface supports the integrity and homeostasis of osteochondral tissue. In addition to its role in native tissue, calcified cartilage promotes osseointegration, which is critical for graft-to-tissue integration in cartilage tissue engineering [17]. Recognizing its importance, researchers have designed scaffolds for osteochondral interface tissue engineering [16,18–20].

In this study, we engineered a bilayer graft of hyaline cartilage (*type II collagen-rich*) and hypertrophic cartilage (*type X collagen-rich*), where type X collagen (COLX) is conducive to mineral deposition for subsequent calcified cartilage formation [21]. Previously, we fabricated a macroporous cryogel based on chondroitin sulfate (CS), modified with arginine-aspartate-glycine (RGD) peptide to provide anchor points for cell adhesion [22]. A natural polymer widely used in cartilage tissue engineering, CS was methacrylated (CSMA) to improve its mechanical strength and resistance to degradation, and to enable crosslinking with acrylated RGD and PEGDA. RGD incorporation showed favorable results for chondrocyte redifferentiation and hyaline cartilage tissue formation. Accordingly, in the current study, we adapted the chondro-conductive RGD-modified cryogel (RGD group) for the upper, hyaline layer. To promote chondrocyte hypertrophy in the bottom layer, we incorporated a Mg^{2+}-containing calcium phosphate called whitlockite (WH: $Ca_{18}Mg_2(HPO_4)_2(PO_4)_{12}$) into RGD-modified cryogel (RGDW group). Our RGD/RGDW bilayer scaffold design is much simple and easier to fabricate and use than most of the abovementioned multilayer and gradient scaffolds. Sharing the same CSMA/PEGDA/RGD backbone, there is only one compositional difference between RGD and RGDW layers. Moreover, our approach uses a single cell source and does not involve the use of exogenous growth factors.

While multiple studies have reported that bioceramics such as HAp [23–26] can induce hypertrophic changes in chondrocytes, this is the first to study the effect of WH on chondrocyte hypertrophy. WH releases Ca^{2+} and PO_4^{3-} ions like HAp, but is unique in its release of Mg^{2+} that enhances WH's osteogenic potential [27]. Studies have demonstrated that Mg^{2+} ions play a role in chondrocyte hypertrophy. Hypertrophic chondrocytes are highly proliferative cells and Mg^{2+} is known to promote chondrocyte proliferation [28]. Increasing extracellular Mg^{2+} concentration activates magnesium transporter 1 (MAGT1)-dependent and transient receptor potential cation channel, subfamily M, member 7 (TRPM7)-dependent influx of ATP for cell proliferation [29]. Dou et al. have reported that Mg^{2+} induces gene expression of COLX in chondrocytes [30]. Given such benefits of Mg^{2+}, Yu et al. demonstrated the benefits of doping bioceramic with Mg^{2+} ion for osteochondral interface engineering [19]. Although the amount of Mg^{2+} is relatively small compared to the base material (Mg^{2+}: Ca^{2+} ion = 1: 9), Mg^{2+}-doped bioceramic showed elevated hypertrophic marker expression and *in vitro* mineralization of chondrocytes compared to its unsubstituted counterpart. Moreover, Yu et al. demonstrated that Mg^{2+}-doped bioceramic induces a larger hypertrophic response than hydroxyapatite and tricalcium phosphate. We anticipate that WH's Mg^{2+} ion release would enhance its ability to induce chondrocyte hypertrophy.

The bottom hypertrophic cartilage matures into calcified cartilage layer, which, apart from its function as the osteochondral interface, forms stable and functional integration with the underlying subchondral bone. Since failure to integrate repair tissue with native tissue is a recurring issue in cartilage tissue engineering [31], a calcified cartilage bottom layer provides the grounds for sustained graft-to-tissue integration and long-term graft success [17]. By regenerating the respective cartilage layers and promoting osseointegration, the hyaline cartilage-hypertrophic cartilage bilayer graft (RGD/RGDW) is expected to facilitate functional and integrative osteochondral defect repair.

2. Materials and methods

2.1. Fabrication of RGD and RGDW cryogels

Methacrylated chondroitin sulfate (CSMA) and YRGDS-PEG-acrylate were prepared according to previously reported protocols [32]. Glycidyl methacrylate (GMA) was conjugated to the hydroxyl group of chondroitin sulfate for methacrylation. 1.0 g of chondroitin sulfate sodium salt (10 % *w/v* in PBS; TCI Chemical) was reacted with 1 mL of GMA (Sigma) for 11 d at RT. Acrylate-PEG-N-hydroxysuccinimide ester (acrylate-PEG-NHS, 3500 MW; Jenkem Technology) was conjugated to the N-terminus of H-Tyr-Arg-Gly-Asp-Ser-OH (YRGDS; BeadTech Inc.) by reacting equal molar ratio of each component in 50 mM sodium bicarbonate buffer (pH 8.2) for 2 h at RT. After the reaction, the products were dialyzed against deionized water using 3.5K MWCO dialysis tubing (Thermofisher), lyophilized, and stored at −20 °C until further use. Syntheses of CSMA and YRGDS-PEG-acrylate were confirmed by ^{1}H NMR [22].

To obtain the gel precursor solution, CSMA, polyethylene glycol diacrylate (PEGDA, 3400 MW; Alfa Aesar) and YRGDS-PEG-acrylate were dissolved in PBS at 5 % (*w/v*), 5 % (*w/v*) and 4 mM, respectively. 40 μL of 10 % (*w/v*) ammonium persulfate (APS; Sigma) and 2 μL of N,N,N′,N'-Tetramethyl ethylenediamine (TEMED; Sigma) were added to 1 ml of the precursor solution and thoroughly mixed. 80 μL of the solution was loaded on pre-cooled cryomolds and placed at −20 °C for overnight cryogelation. Cryogels were then lyophilized for 2–3 h. WH, synthesized as described previously [27], was incorporated into the precursor solution prior to addition of APS and TEMED at 1 % (*w/v*) to fabricate RGDW cryogels.

To create RGD/RGDW bilayer cryogels, 40 μL of RGDW solution was loaded first as the bottom layer and placed at −20 °C for 30 min. Then, equal volume of RGD solution was added on top of the RGDW layer and placed at −20 °C for overnight cryogelation. For visualization of the distinct layers, CSMA was stained with either Safranin-O (Polysciences)

for red color or Alcian Blue (Polysciences) for blue color and used for fabrication of RGD and RGDW layers, respectively.

2.2. Characterization of RGD and RGDW cryogels

Cryogels were swelled in PBS for 24 h and then snap frozen in liquid nitrogen and lyophilized for SEM imaging. After gold sputtering, SEM images of the cryogel macroporous structure were acquired at 5.0 kV using JSM-7800F Prime (JEOL Ltd.). Cryogel pore size was quantified using ImageJ software. WH nanoparticles were also imaged using SEM and their particle size was calculated from SEM images using ImageJ (3 different fields, 300 particles).

To determine the degree of swelling, cryogels were weighed twice, once after reaching equilibrium swelling in PBS ($W_{swollen}$) and once after lyophilization (W_{dry}). The equilibrium swelling ratio (Q) was calculated using the following equation: $Q = (W_{swollen} - W_{dry})/W_{dry} \times 100$. Young's moduli of the cryogels were measured via compressive mechanical testing. Cryogels at equilibrium swelling were subjected to compression at a constant strain rate of 1 mm/min using EZ-SX STD (Shimadzu). To obtain stress *vs.* strain graph, load *vs.* displacement data was normalized by dimensions of the cryogel. Young's modulus was determined from the linear region of stress *vs.* strain graph.

Ion release profile of Ca^{2+}, Mg^{2+}, and PO_4^{3-} from WH-containing cryogel was analyzed. WH-containing cryogels ($N = 4$) were incubated in 1 mL of deionized water at RT. The incubated solution was collected at each time point and replenished with fresh water. Each sample was analyzed via inductively coupled plasma atomic emission spectrometer (ICP-AES, OPTIMA 8300, PerkinElmer) with argon plasma.

2.3. Isolation and culture of chondrocytes

Knee joints from freshly slaughtered pigs were obtained from a local slaughterhouse. Under laminar flow hood, thin chips of hyaline cartilage were removed from the cartilage surface and finely minced into <1 mm^3 chunks. The minced tissue was subsequently digested with 0.15 % (*w/v*) type II collagenase (Worthington) for 18 h under constant rotation at 37 °C. The tissue digest was passed through a 70 μm cell strainer to eliminate cell debris and centrifuged. The cell pellet was washed twice with PBS and then, cultured in high glucose Dulbecco's modified Eagles' medium (Hyclone), supplemented with 10 % (*v/v*) fetal bovine serum (Corning), 1 % (*v/v*) penicillin/streptomycin (Gibco), 1 % (*v/v*) non-essential amino acid (Gibco), 1 % (*v/v*) 4-(2-hydroxyethyl)-1-piperazineethanesulfonic acid (Gibco), 20 μg/mL L-ascorbic acid (Sigma), and 8 μg/mL L-proline (Sigma). Cell culture was maintained at 37 °C and 5 % CO_2 with media change every 3 days. Chondrocytes at passage 1 were used for the entire study.

2.4. Cell response to Mg^{2+} ion

Chondrocytes (P1) were harvested with 0.25 % trypsin-ethylenediaminetetraacetic acid (trypsin-EDTA; Gibco) and centrifuged at 1100 rpm to remove trypsin-EDTA. Subsequently, chondrocytes were seeded in 96 well plate at a density of 10,000 cells/cm^2. On the following day, each well was treated with 100 μL of serum-free media containing 0–5 mM $MgCl_2$ (Invitrogen). PrestoBlue assay was conducted on day 3 of Mg^{2+} treatment, according to manufacturer's instruction. Real time PCR and immunostaining were conducted on day 7 and day 14, respectively, to observe chondrocyte hypertrophy-related gene and protein expression changes due to Mg^{2+} ion (refer to sections 2.7 and 2.11 for experimental procedure).

2.5. Preparation of cell-seeded cryogels

Prior to cell seeding, cryogels were thoroughly washed with PBS overnight to remove APS and TEMED, and sterilized in 70 % ethanol for 1 h. After removing ethanol, cryogels were thoroughly washed with sterile PBS and blotted with UV-sterilized Kimtech. Chondrocytes were harvested with 0.25 % trypsin-EDTA and centrifuged to obtain a cell pellet. The cell pellet was resuspended in culture media at a concentration of 100M cells/mL. Next, 50 μL of the cell suspension was seeded onto each cryogel (5M cells/construct) and incubated at 37 °C for 2 h to allow cell attachment. Chondrocyte-seeded cryogels were maintained at 37 °C and 5 % CO_2 with media change every 2–3 days.

2.6. Cell viability and proliferation test

Chondrocyte viability and proliferation in RGD or RGDW cryogel were observed using Live/Dead™ Viability/Cytotoxicity (Invitrogen), Cell Counting Kit 8 (CCK-8; Dojindo Laboratories) and Quant-iT™ PicoGreen™ dsDNA Assay Kit (Invitrogen). Chondrocytes were seeded in sterilized cryogels at a density of 0.1M (live/dead) or 0.5M (CCK-8, PicoGreen) cells/construct. To observe initial cell viability, cells were stained with Calcein AM (green)/Ethidium homodimer-1 (red) solution, according to manufacturer's instruction. Live green and dead red fluorescent cells were imaged using NIS-BR (Nikon).

For proliferation test, CCK-8 reagent was mixed with culture media at a ratio of 1:10, and 1 mL of the solution was added to each chondrocyte-seeded cryogel. After 3 h incubation at 37 °C, absorbance was measured at 450 nm using microplate reader (Tecan). CCK-8 assay was repeated every 3 days, up to d7. For PicoGreen assay, chondrocyte-seeded constructs were collected on week 3 and lyophilized. Samples were mechanically crushed using a pestle and digested in 500 μL of diluted papain solution (41.7 mgP/mL; Worthington Biomedical) for 16 h at 60 °C. DNA content was quantified via Quanti-iT PicoGreen dsDNA assay kit (Invitrogen), according to the manufacturer's instruction. Standard curve was constructed from fluorescence values of known DNA concentrations to calculate DNA content of samples.

2.7. Real-time PCR analysis of gene expression

Total RNA was extracted from chondrocyte-laden cryogels with TRIzol reagent (Invitrogen), and cDNA was synthesized from the RNA using M-MLV cDNA Synthesis kit (Enzynomics) following the manufacturer's instruction. Real-time PCR analysis was performed using SYBR Green PCR Mastermix (Enzynomics) and ABI StepOnePlus Real-Time PCR system (Applied Biosystems), with glyceraldehyde-3-phosphate dehydrogenase (GAPDH) as the housekeeping gene. The expression level of each target gene was calculated as $-2^{\Delta\Delta Ct}$. PCR primer sequences used are listed in Table 1.

2.8. Subcutaneous implantation

To minimize animal suffering, all procedures were performed under anesthesia using Alfaxan (Jurox) and Rompun (Bayer). Female 8 weeks-old Balb/c nude mice ($N = 4$) were used to assess *in vivo* ectopic cartilage

Table 1
List of porcine PCR primers.

Gene	Type	Primer 5' - 3'
GAPDH	housekeeping	F: TGAAGGTCGGAGTGAACGGAT R: CACTTTGCCAGAGTTAAAAGCA
COL2	chondrogenic	F: GAGAGGTCTTCCTGGCAAAG R: AAGTCCCTGGAAGCCAGAT
ACAN	chondrogenic	F: CGAAACATCACCGAGGGT R: GCAAATGTAAAGGGCTCCTC
RUNX2	hypertrophic	F: CAGAAGGCACAGACAGAAGC R: AGGACTTGGTGCAGAGTTCA
COLX	hypertrophic	F: TGACCCTGGAATTGGAGGAC R: GACCAGGAGGACCTGGATTT
MMP13	hypertrophic	F: GGTCTGTTGGCTCATGCTTT R: GGTCCTTGGAGTGGTCAAGA
COL1	dedifferentiated	F: GAGGATGGTCACCCTGGAAA R: TAATGCCCTTGAAGCCAGGA

formation. Chondrocyte-laden RGD and RGDW cryogels (5M cells/construct) were subcutaneously implanted in the mice. After 6 weeks, animals were euthanized using CO_2 gas injection, and samples were collected for mechanical, histological and immunostaining analyses.

2.9. Mouse cranial defect model

Cranial defect model was created in female 8 weeks-old Balb/c nude mice ($N = 4$) to assess cartilage mineralization via hypertrophic chondrocytes. A scalp incision was made along the mid-sagittal plane and a critical-sized 4-mm diameter defect was created using a surgical drill (STRONG 106, Saeshin). Then, the following groups of cryogels (with or without chondrocyte (ccty)) were implanted into the defect site: RGD-ccty (control), RGDW-ccty, RGD + ccty and RGDW + ccty. After 6 weeks, mice were sacrificed using CO_2 gas injection and their cranial cavities were collected for micro-CT and histological analyses.

2.10. Rabbit osteochondral defect model

Prior to surgery, rabbit chondrocytes were isolated from rabbit articular cartilage using the same protocol in section 2.3 and seeded in RGD and RGD/RGDW cryogels (diameter: 4 mm, height: 3 mm). Ten male New Zealand white rabbits (~2.5 kg) were used for the implantation study. Osteochondral defects were created bilaterally and randomly assigned to three groups: Defect only ($N = 6$), RGD ($N = 7$) and RGD/RGDW ($N = 7$). Rabbits were sedated with intramuscular injection of Alfaxan and Rompun and anesthetized with isofluorane (Ifran, Hana Pharm Co.) of 3 MAC for induction and 1.5–2 MAC for maintenance with 1~2 L/min O_2 flow. The outer skin was first disinfected with chlorhexidine-alcohol solution. The skin and joint capsule were incised via medial parapatellar approach and the patella was dislocated laterally to expose the patellar groove. An osteochondral defect (diameter: 4 mm, height: 3 mm) was created on the femoral trochlear groove using the surgical drill and implanted with the respective cell-seeded construct (RGD or RGD/RGDW) or left empty (Defect only). After moving the patella back in place, the joint capsule was sutured using an absorbable 4-0 suture (Ethicon) and the outer skin was closed with a 2-0 black silk suture (Ailee). Postoperatively, rabbits received subcutaeneous injections of antibiotics (Triaxone, 25 mg/kg; Hanmi) and analgesics (Tramadol HCl, 5 mg/kg; HanAll Biopharma) for 5 days. At 12 weeks post-surgery, the rabbits were sacrificed using CO_2 gas injection and femoral heads were collected for microCT and histological analyses. Histological sections were blind-scored using International Cartilage Repair Society (ICRS) II scoring as shown in Table 2.

2.11. Histological analysis

Upon collection, samples were fixed in 4 % PFA for overnight, paraffin-embedded and sectioned at 3 μm thickness. Prior to paraffin embedding, mouse cranial cavities and rabbit femoral heads were decalcified with 10 % ethylenediaminetetraacetic acid (EDTA; MBcell) for 1 and 4 weeks under gentle shaking at 4 °C.

Slides were deparaffinated in xylene, rehydrated in graded ethanol series and stained according to the following protocols. In H&E staining, Mayer's Hematoxylin (Vector Laboratories) and Eosin Y (Sigma Aldrich) were stained for 5 min and 30 s, respectively. In Safranin-O staining, Hematoxylin and Safranin-O (Polysciences) were stained for 5 min and 7 min, respectively. Masson's trichrome (MTC) staining (Polysciences) involved 8 min of Weigert's Hematoxylin, 5 min of Biebrich Scarlet-Acid Fuchsin, and 5 min of Aniline Blue. Stained slides were dehydrated in graded ethanol series and mounted with canada balsam (Sigma). Images were captured using NIS-BR (Nikon).

2.12. Immunostaining analysis

After antigen retrieval with proteinase K (Sigma) for 10 min at 37 °C, slides were cell-permeabilized with 0.1 % Triton-X and blocked with 10 % (*v/v*) goat serum for 2 h at RT. The slides were then incubated with primary antibody against collagen I (1:100 dilution, ab34710 (Abcam) or MA1-26771 (Invitrogen)), collagen II (1:100 dilution, ab34712 (Abcam) or BS-0709R (Bioss)), collagen X (1:100 dilution, ab49945 (Abcam)), matrix metallopeptidase 13 (1:200 dilution, ab219621 (Abcam)), osteocalcin (1:150 dilution, ab13418, Abcam), runt-related transcription factor 2 (1:200 dilution, sc-390351 (Santa Cruz)), and SRY-Box Transcription Factor 9 (1:100 dilution, ab185966 (Abcam)) overnight at 4 °C. The slides were washed to remove any unbound primary antibody and incubated with goat anti-mouse or goat anti-rabbit antibody (1:500 dilution, A21151 or A11008, Invitrogen) for 90 min at RT. DAPI was applied at 1:200 dilution for 10 min. Immunostained slides were imaged using NIS-BR and analyzed (mean fluorescence intensity or number of positive cells) using ImageJ.

Table 2
International Cartilage Repair Society (ICRS) II scoring system.

Histological parameter	Score
1. Tissue morphology	0 %: Full-thickness collagen fibers 100 %: Normal cartilage birefringence
2. Matrix staining	0 %: No staining 100 %: Full metachromasia
3. Cell morphology	0 %: No round/oval cells 100 %: Mostly round/oval cells
4. Chondrocyte clustering (4 or more grouped cells)	0 %: Present 100 %: Absent
5. Surface architecture	0 %: Delamination or major irregularity 100 %: Smooth surface
6. Basal integration	0 %: No integration 100 %: Complete integration
7. Formation of a tidemark	0 %: No calcification front 100 %: Tidemark
8. Subchondral bone abnormalities/marrow fibrosis	0 %: Abnormal 100 %: Normal marrow
9. Inflammation	0 %: Present 100 %: Absent
10. Abnormal calcification/ossification	0 %: Present 100 %: Absent
11. Vascularization (within the repaired tissue)	0 %: Present 100 %: Absent
12. Surface/superficial assessment	0 %: Total loss or complete disruption 100 %: Resembles intact articular cartilage
13. Mid/deep zone assessment	0 %: Fibrous tissue 100 %: Normal hyaline cartilage
14. Overall assessment	0 %: Bad (fibrous tissue) 100 %: Good (hyaline cartilage)

2.13. Micro-computed tomography

The degree of bone formation was evaluated using SkyScan 1172 (Bruker) for mouse cranial defect experiment and Quantum GX2 (PerkinElmer) for rabbit osteochondral defect experiment. Operation source voltage and current were 59 kV and 167 μA (mouse cranial defect) and 90 kV and 89 μA (rabbit osteochondral defect). Micro-CT images were analyzed using analysis program of each manufacturer. After setting the region of interest (ROI), the extent of bone regeneration was expressed as percentage of bone volume over total ROI volume (% BV/TV).

2.14. Statistics

All data are presented as mean ± standard deviation (SD). For statistical analysis, two-tailed t-tests or one-way analysis of variance (ANOVA) with Tukey's post hoc tests were performed on GraphPad software. Statistical significance was considered for $^{*}p < 0.05$, $^{**}p < 0.01$ and $^{***}p < 0.005$, $^{****}p < 0.0001$.

3. Results

3.1. Characterization of cryogels

Whitlockite (WH), a magnesium-containing calcium phosphate, was incorporated into RGD cryogel to produce hypertrophic cartilage. WH nanoparticles used in this study were imaged using SEM and have an average size of 32.16 ± 11.07 nm (Supplementary Fig. 1). RGD and RGDW groups were separately evaluated for *in vitro* chondrocyte culture and *in vivo* mouse subcutaneous implantation and cranial defect studies, and arranged as a bilayer for implantation into rabbit osteochondral defect model (refer to 'Graphical Abstract').

RGD and RGDW cryogels were fabricated via cryogelation process in Fig. 1A and visualized via macroscopic observation and SEM imaging (Fig. 1B). RGDW cryogel appears more opaque and whiter than RGD cryogel, due to the incorporation of 1 % (*w/v*) WH. SEM image shows WH microparticles bound to RGDW cryogel pore walls. There was no significant difference between average pore size and swelling ratio of the two groups (Fig. 1C–D). However, compressive modulus of RGDW cryogel was significantly higher than that of RGD cryogel (Fig. 1C). Addition of WH mechanically reinforced the RGDW cryogel, but did not affect its crosslinking density.

The ion release profiles of Ca^{2+}, Mg^{2+}, and PO_4^{3-} from RGDW cryogel were monitored up to 4 weeks (Fig. 1F). PO_4^{3-} release rate already plateaued by week 2, while release of Ca^{2+} and Mg^{2+} began to slow down after 3 weeks. The expedited release of negatively charged PO_4^{3-} ion may be attributed to electrostatic repulsion to negatively charged chondroitin sulfate in the cryogel backbone. Accumulative release of Ca^{2+}, Mg^{2+}, and PO_4^{3-} on week 4 were 26.3 ± 3.2 mg/L, 4.6 ± 0.5 mg/L and 51.0 ± 5.3 mg/L, respectively. Accumulative release amounts of Ca^{2+} (0.65 mM) and PO_4^{3-} (0.54 mM) were noticeably higher than that of Mg^{2+} (0.19 mM), given the relative abundance of Ca^{2+} and PO_4^{3-} in WH ($Ca_{18}Mg_2(HPO_4)_2(PO_4)_{12}$).

Then, we fabricated RGD(red)/RGDW(blue) bilayer cryogel and applied compressive force on it using forceps (Supplementary Data Movie S1). RGD/RGDW cryogel recovered its shape after multiple compressions and maintained its distinct bilayer with no separation between the layers (Fig. 1G).

Supplementary video related to this article can be found at https://doi.org/10.1016/j.bioactmat.2024.06.018

3.2. Influence of WH on chondrocyte hypertrophy (in vitro)

First, we examined the effect of WH on cryogel-seeded chondrocytes *in vitro*. No initial cytotoxicity was observed in RGD and RGDW cryogels (Fig. 2A). Absorbance value from Cell Counting Kit-8 assay was significantly higher for RGDW group than RGD group on day 7 (Fig. 2B). DNA content, which is proportional to cell number, per cryogel was also significantly higher for RGDW group on day 21 ($p < 0.01$, Fig. 2C). Chondrogenic gene (*COL2* and *ACAN*) expression of RGDW group decreased throughout the culture period and were significantly lower than that of RGD group on weeks 2 and 3 (Fig. 2D–E). Expression of

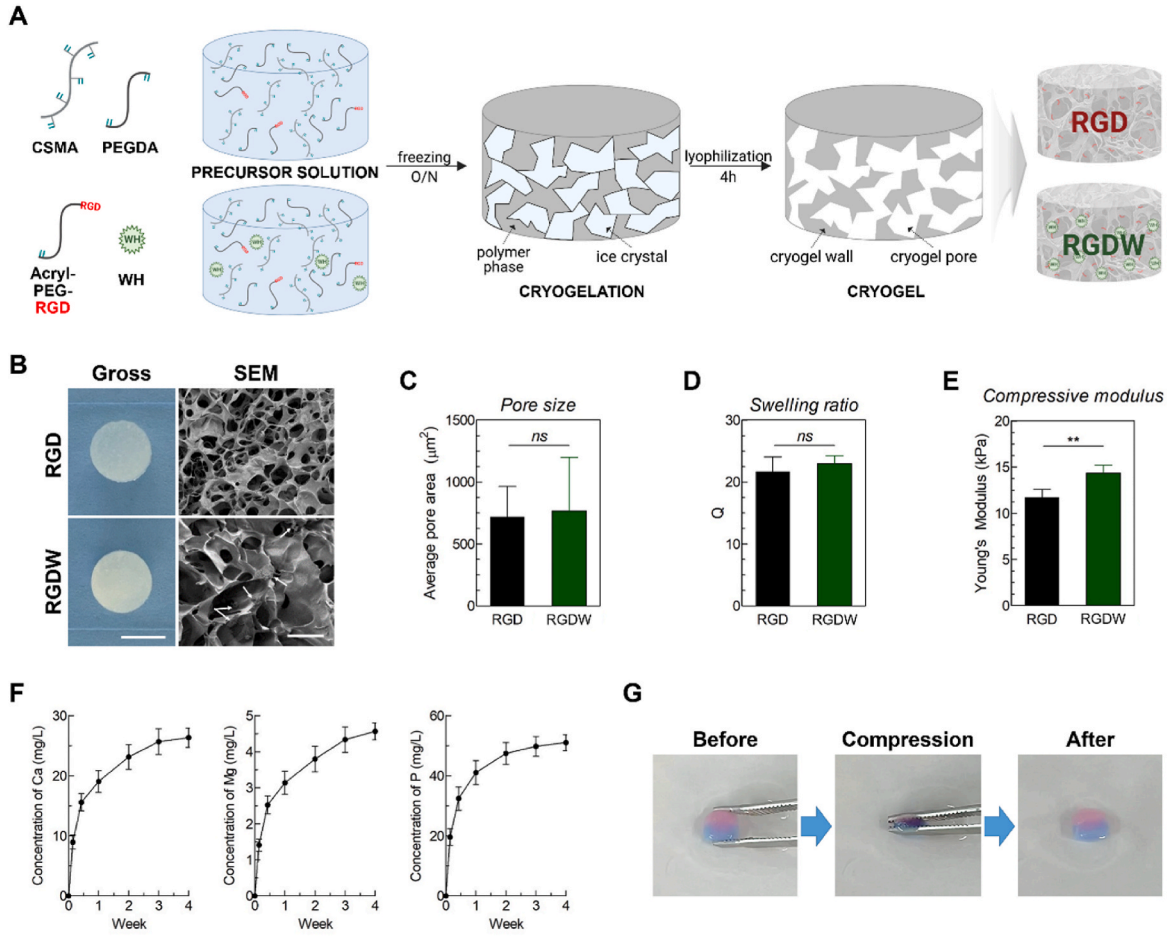

Fig. 1. Preparation and characterization of RGD and RGDW cryogels. (A) Cryogel fabrication process. (B) Gross appearance and SEM image. White arrows in SEM image indicate WH particles that are bound to the cryogel wall. Scale bar = 5 mm (macroscopic image), 100 μm (SEM). (C) Average pore area of lyophilized cryogels. (D) Swelling ratio. (E) Young's modulus determined from compressive testing. (F) ICP-AES result of Ca^{2+}, Mg^{2+}, and PO_4^{3-} ion released from RGDW cryogels with time. (G) Compressed RGD(red)/RGDW(blue) bilayer cryogel can return to the original shape. Error bars indicate standard deviation (SD). $N = 4$. **p < 0.01.

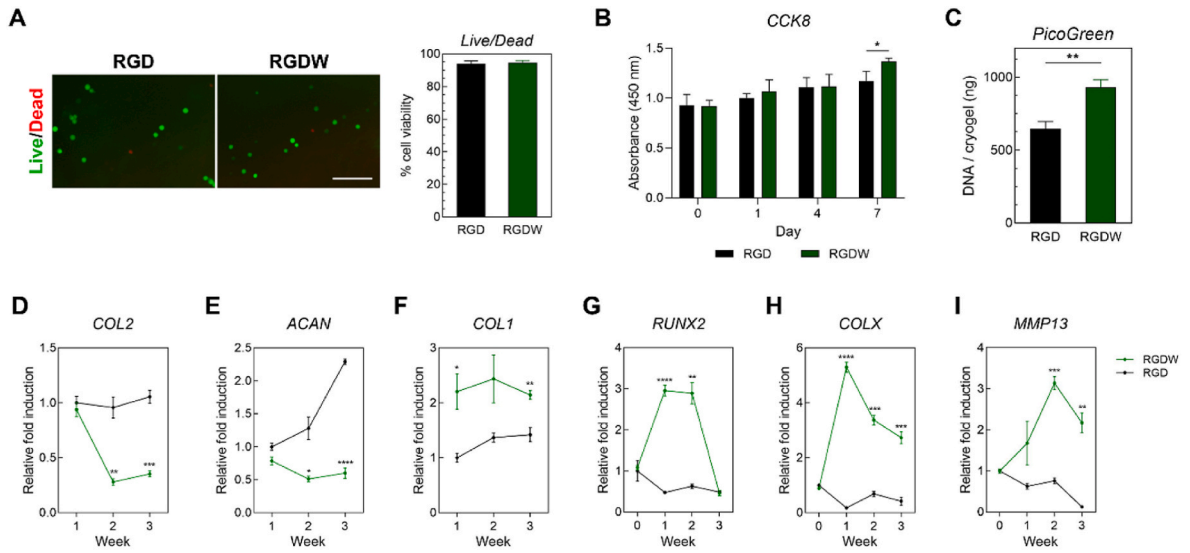

Fig. 2. WH induces chondrocyte hypertrophy in RGDW cryogels. (A) Live/dead assay at 24 h. Scale bar = 50 μm. (B) CCK8 assay on day 7. (C) PicoGreen dsDNA assay on week 3. (D–I) Real-time PCR results of (D–E) chondrogenic (*COL2*, *ACAN*) and (F) chondrocyte dedifferentiation (*COL1*) markers, (G–I) hypertrophy-related (*RUNX2*, *COLX*, *MMP13*) markers. Error bars indicate SD. $N = 4$. *p < 0.05, **p < 0.01, ***p < 0.005, ****p < 0.0001, compared to RGD group.

COL1, a marker of chondrocyte dedifferentiation, was slightly higher in RGDW group (Fig. 2F). An important inducer of chondrocyte hypertrophy [33], *RUNX2* gene expression of RGDW group was upregulated by 3 folds on weeks 1 and 2 and returned to day 0 level on week 3 (Fig. 2G). Expression level of hypertrophic gene *COLX* peaked on week 1 (5.3-fold, relative to day 0) and remained significantly higher compared to control (Fig. 2H). A key ECM-degrading enzyme that accompanies *COLX* expression, *MMP13* gene expression level of RGDW group reached its peak a week later (Fig. 2I). In RGD group, *RUNX2*, *COLX*, and *MMP13* expression levels steadily decreased with time.

Week 3 *in vitro* samples were immunostained for chondrogenic and hypertrophic markers. SOX9, the master transcription factor in chondrogenesis, is constitutively expressed in chondrocytes, and its expression is typically downregulated during chondrocyte hypertrophy [34]. SOX9 protein expression, detected in RGD group, was almost absent in RGDW group (Fig. 3A). COL2 expression was also downregulated in RGDW group compared to RGD group (Fig. 3B). COLX and MMP13 protein expressions were significantly upregulated in RGDW group (Fig. 3C–D). Through real-time PCR and immunostaining, we confirmed that chondrocytes experience hypertrophic changes in RGDW cryogels.

Chondrocyte hypertrophy-inducing effects of Ca^{2+} and PO_4^{3-} ions are well-documented in previous studies [35–38]. Here, we examined whether Mg^{2+}, another major ion released by WH, also plays a role in chondrocyte hypertrophy. Presto blue viability assay was performed to

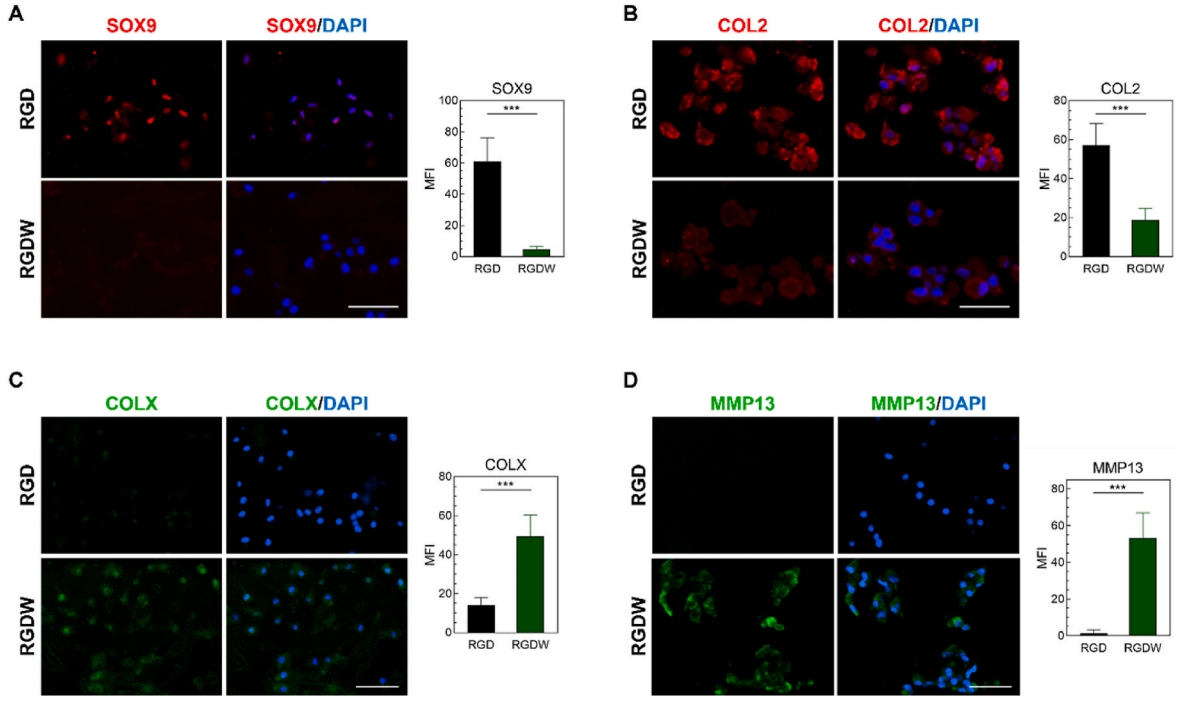

Fig. 3. Chondrocytes exhibit hypertrophy-related protein expression changes in RGDW cryogels. Immunostaining and fluorescence intensity quantification of (A) SOX9, (B) COL2, (C) COLX, (D) MMP13. Scale bar = 50 μm. Error bars indicate SD. $N = 4$. ***p < 0.005.

observe the effect of Mg^{2+} on cell viability and proliferation since hypertrophic chondrocytes are highly proliferative cells. As expected, cell viability increased with the rise in Mg^{2+} concentration (Supplementary Fig. 2A). In general, expression levels of *COLX* and *MMP13* genes increased and *COL2* gene decreased in Mg^{2+} concentration-dependent manner (Supplementary Fig. 2B). In line with *COLX* gene expression, COLX immunocytochemistry also showed the highest level of protein expression at 2 mM Mg^{2+} group (Supplementary Fig. 2C). However, to note, COLX gene and protein expressions were decreased at 5 mM Mg^{2+}, suggesting that there is an optimal dose for Mg^{2+} ion treatment. We confirmed that the total amount of Mg^{2+} ions released (concentration * volume) from RGDW cryogels (1 % *w/v* WH) corresponds to the total amount of Mg^{2+} ions in 2 mM group.

3.3. WH-mediated hypertrophic cartilage formation in mouse subcutaneous implantation model

We then evaluated hypertrophy-inducing effect of WH *in vivo*. Chondrocyte-laden RGD and RGDW cryogels were collected and analyzed after 6 weeks of subcutaneous implantation in mice (Fig. 4A). Compressive modulus of RGDW group was significantly greater (1.8 times, $p < 0.01$) than that of RGD group (Fig. 4B). We performed immunostaining and real-time PCR to assess protein and gene expression of chondrogenic and hypertrophy-related markers. RGD group exhibited strong COL2 expression and no COLX and MMP13 expression, a phenotype of articular chondrocytes (Fig. 4C–D). In contrast to RGD group, RGDW group showed abundant COLX and MMP13 protein expression and weak COL2 expression, a phenotype of hypertrophic chondrocytes. Mean fluorescence intensity (MFI) was significantly different ($p < 0.0001$) for all markers. Similar trend was observed in gene expression levels. *COL2* and *ACAN* gene expressions were downregulated by 5 folds and 3 folds in RGDW group compared to RGD group (Fig. 4E). In RGDW group, *COLX*, *MMP13*, and *RUNX2* expressions were upregulated by 17 folds, 12 folds, and 1.5 folds, respectively (Fig. 4F). Chondrocyte-laden RGD/RGDW bilayer scaffold showed distinct COL2/COLX expressions within their respective layers (Fig. 4G). Through *in vitro* and *in vivo* studies, we demonstrated that WH drives chondrocyte hypertrophy and COLX accumulation for hypertrophic cartilage formation.

3.4. WH-induced hypertrophic cartilage mineralizes in bone microenvironment

To confirm the mineralization of our tissue engineered hypertrophic cartilage, we implanted chondrocyte-laden RGDW cryogels in a mouse critical-sized cranial defect for 6 weeks (Fig. 5). The following groups of cell-laden (+ccty) or cell-free (-ccty) RGD and RGDW cryogels were evaluated: RGD-ccty (control), RGDW-ccty, RGD + ccty and RGDW + ccty. Although primarily used for bone imaging, microCT can also visualize mineral deposits in calcified cartilage [39]. In microCT analysis, RGDW + ccty group exhibited the highest degree of defect filling with mineralized neotissue—6 times higher than control and statistically significantly higher ($p < 0.01$) than the other groups (Fig. 5A). Notably, mineralized tissue formation was negligible in defect sites

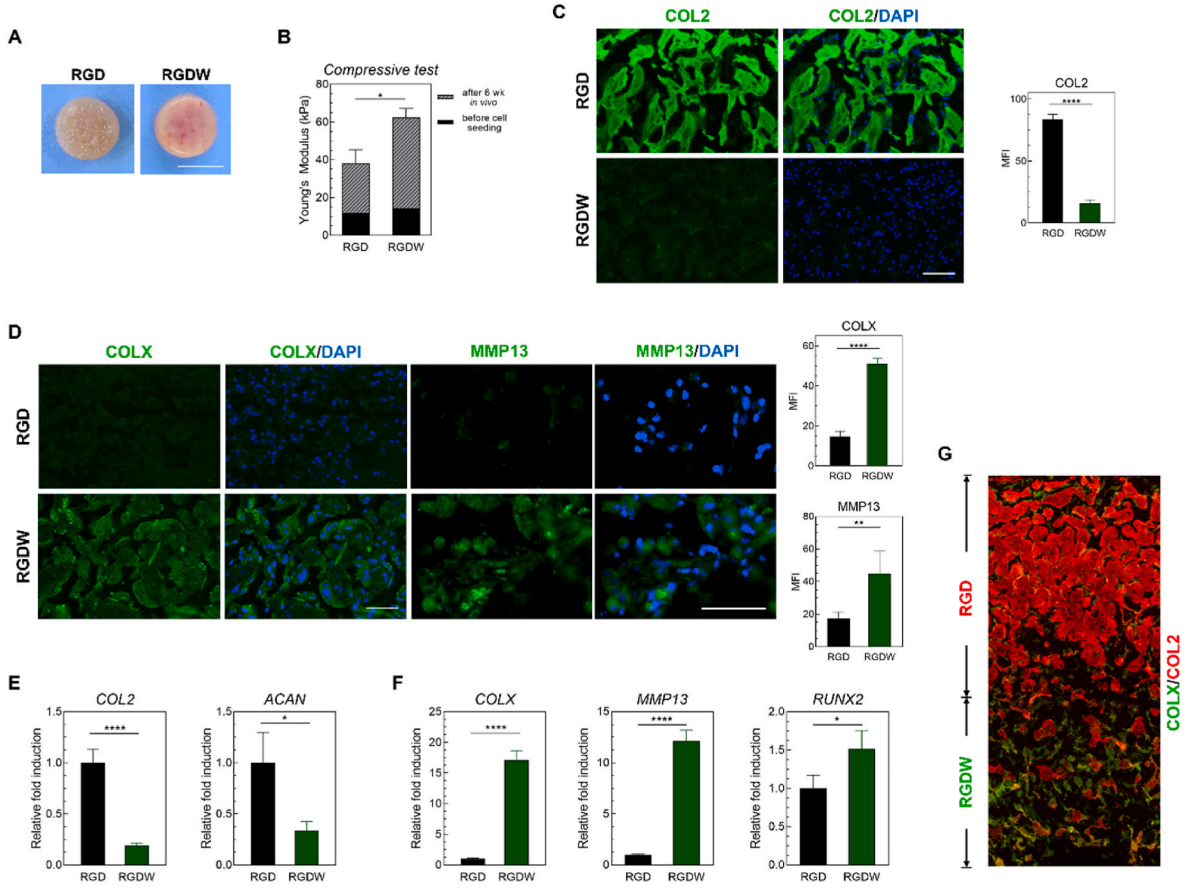

Fig. 4. WH induces ectopic hypertrophic cartilage formation. (A) Macroscopic appearance of chondrocyte-seeded constructs after 6 weeks of *in vivo* subcutaneous implantation. Scale bar = 5 mm. (B) Compressive modulus of RGD and RGDW groups, before and after *in vivo* culture. (C) Immunostaining and quantification of COL2. Scale bar = 50 μm. (D) Immunostaining and quantification of COLX and MMP13. Scale bar = 50 μm. (E) Real-time PCR analysis of chondrogenic markers *COL2* and *ACAN*. (F) Real-time PCR analysis of hypertrophic markers *COLX, MMP13*, and *RUNX2*. (G) COL2/COLX double immunostaining of RGD/RGDW bilayer scaffold. Error bars indicate SD. $N = 4$. *$p < 0.05$, **$p < 0.01$, ****$p < 0.0001$.

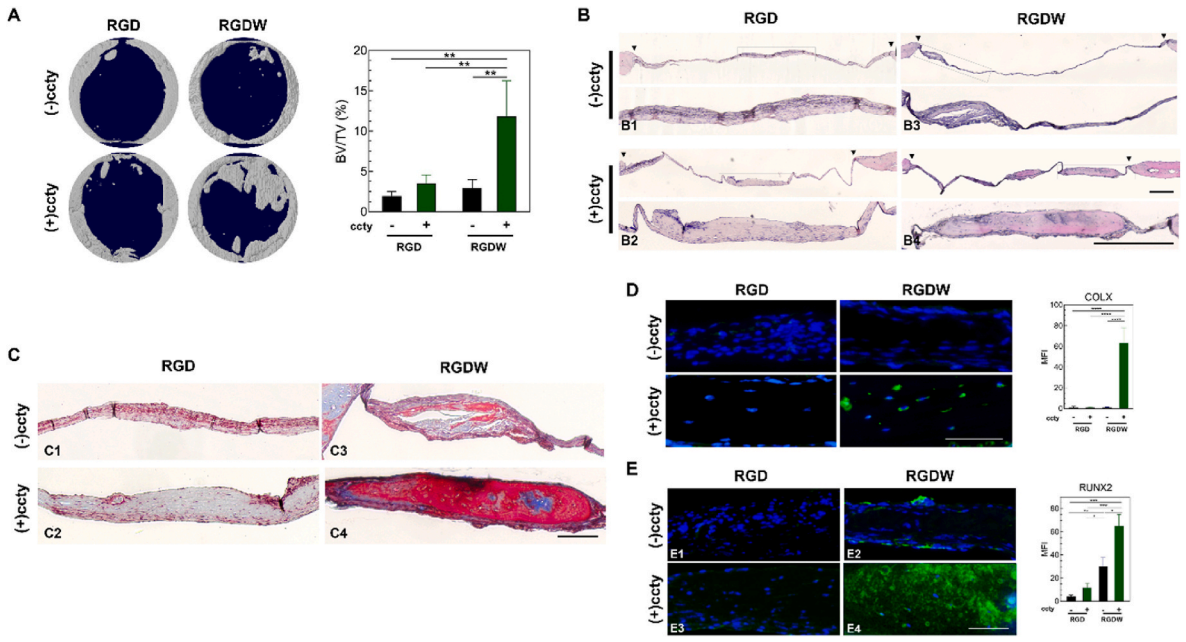

Fig. 5. Hypertrophic cartilage mineralizes in mouse cranial defect model. (A) Micro-CT scan of cranial defects implanted with RGD or RGDW cryogel that are seeded with or without chondrocytes (± ccty) at 6 weeks. Neotissue formation is indicated as percentage of new bone volume/total bone volume (% BV/TV) in defect area. (B) H&E staining. Black triangles mark the boundaries of the cranial defect. Scale bar = 250 μm. (C) Masson's Trichrome staining. Scale bar = 100 μm. (D–E) Immunostaining and quantification of COLX and RUNX2 expression. Scale bar = 50 μm. Error bars indicate SD. $N = 4$. *p < 0.05, **p < 0.01, ***p < 0.005.

implanted with non-hypertrophic chondrocytes (RGD + ccty group) or bioceramic-containing scaffold without hypertrophic chondrocytes (RGDW-ccty group).

We performed histological (H&E, MTC) staining and immunostaining on cranial defect samples to observe the quality of neotissue. In MTC staining, Acid Fuchsin (with affinity to mineralization) positively stains mineralized tissue in red, while Aniline Blue stains non-mineralized collagen fibers in blue. Little bone formation was observed within the cranial defects of RGD-ccty and RGD + ccty groups. In these groups, a fibrous periosteal tissue had formed, bridging the defect (Fig. 5B1-2,

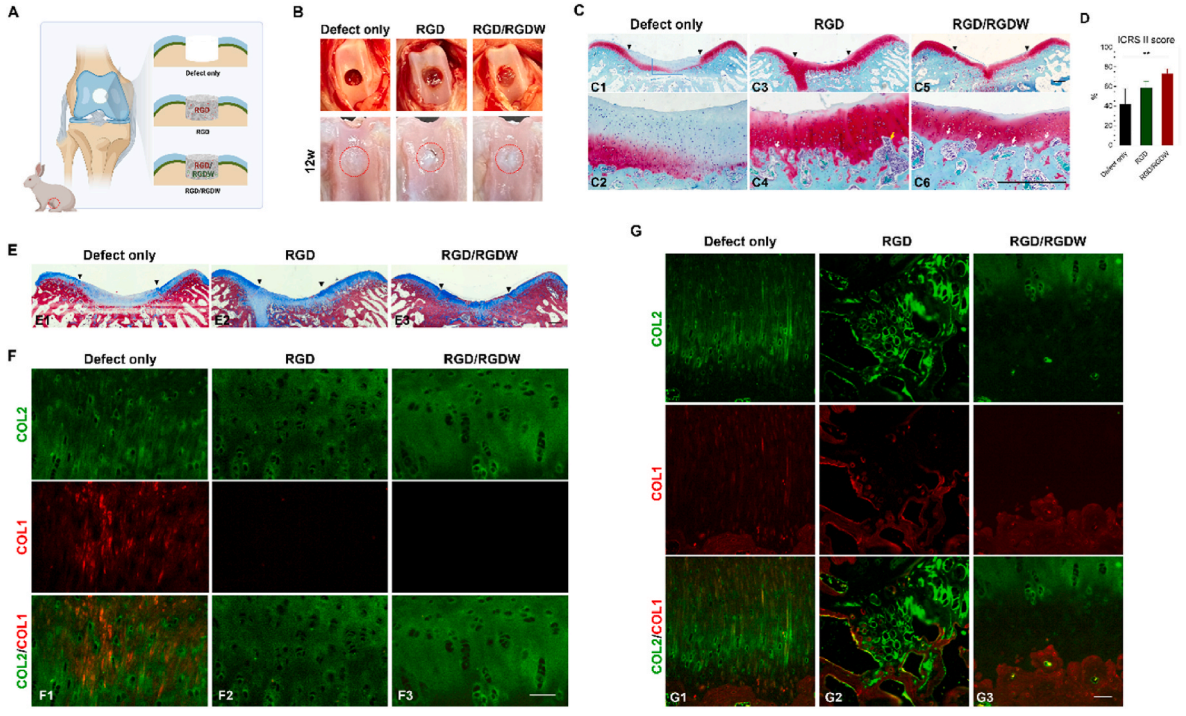

Fig. 6. RGD/RGDW bilayer promotes osteochondral defect repair. (A) Experimental scheme of rabbit osteochondral defect model. (B) Macroscopic appearance of defect site on surgery day and after 12 weeks. (C) Safranin-O staining, whole image and zoomed in image. Black triangles mark the boundaries of the defect area. White arrows indicate tidemark and yellow arrows indicate vascular infiltration. Scale bar = 500 μm. (D) International Cartilage Repair Society (ICRS) II scoring. (E) Masson's trichrome staining. Scale bar = 500 μm. (F–G) Double immunostaining of COL2/COL1 of (F) regenerated cartilage tissue and (G) cartilage-bone interface. Scale bar = 50 μm. Error bars indicate SD. **p < 0.01.

5C1-2). While most of the defect area was covered by fibrous periosteal tissue (Fig. 5B3), RGDW-ccty group had a small piece of neotissue stained in red and blue on the periphery of the defect area, adjacent to the native cranial tissue (Fig. 5C3). The regenerated tissue of RGDW + ccty group exhibited intense red staining with limited blue area in MTC staining (Fig. 5C4) and the highest expression level of RUNX2 (Fig. 5E). COLX-positive cells were only detected in RGDW + ccty group (55.7 ± 8.3 % of total number cells) (Fig. 5D). Osteocalcin (OCN) expression, which is found in mature cranial bone, was absent in all groups (Supplementary Fig. 3). These results showed that chondrocyte-laden RGDW cryogel mineralizes in bone microenvironment.

3.5. RGD/RGDW bilayer in rabbit osteochondral defect model

Osteochondral defect in rabbit femoral trochlear groove was implanted with chondrocyte-laden RGD or RGD/RGDW scaffold, or left empty (Defect only) (Fig. 6A). After 12 weeks of implantation, femoral cartilage was collected for microCT and histological analyses. Upon macroscopic examination, Defect only group and RGD/RGDW group exhibited complete filling and good integration with native tissue, while a large fissure was observed in RGD group (Fig. 6B). Repaired tissue of RGD group and RGD/RGDW group was glossy and translucent like hyaline cartilage, whereas that of Defect only group was opaque and fibrocartilage-like in appearance.

In Safranin-O staining, Defect only group showed partial staining for sulfated glycosaminoglycans (sGAG) (Fig. 6C1); pericellular lacunae, a feature of hyaline cartilage, were not observed in the non-stained area (Fig. 6C2). This result confirms that tissue filling in macroscopic view is not hyaline cartilage. RGD group showed strong red staining for sGAG, but the stained region extended into the subchondral region (Fig. 6C3). RGD/RGDW group showed strong sGAG staining that was confined to the articular cartilage layer (Fig. 6C5). Formation of tidemark, a thin line marking the boundary between hyaline and calcified cartilage, was observed in RGD/RGDW group (white arrow), but not in RGD group (Fig. 6C4, 6C6). Moreover, vascular infiltration into avascular, non-calcified cartilage zone was observed in RGD group (yellow arrow), while vascularization was limited to the calcified cartilage zone and subchondral bone in RGD/RGDW group. Histological sections were blind-scored using ICRS II scoring system, a comprehensive scoring system comprised of 14 parameters as shown in Table 2. Defect only (control) group had the lowest score, with significant difference ($p < 0.01$) compared to RGD/RGDW group (Fig. 6D). Score of RGD/RGDW group (73.2 ± 4.9 %) was also higher than that of RGD group (58.9 ± 6.6 %).

We observed similar staining patterns in MTC staining (collagen) as in Safranin-O staining (sGAG). Repaired tissue in Defect only group displayed lighter blue staining for collagen (Fig. 6E1). Blue repaired tissue in RGD group extended deep into the subchondral region, while blue staining was relatively well-confined to the articular cartilage layer in RGD/RGDW group (Fig 6E2-3). Then, we took a closer look at the type of collagen that constitute the repaired neotissue by performing double immunostaining of COL2 and COL1. COL2 is a marker for hyaline cartilage and COL1 is a marker for fibrous cartilage and bone. We assessed 1) the quality of regenerated cartilage tissue (hyaline, fibrous or mixed) in the articular cartilage layer and 2) the separation between hyaline cartilage and bone at the osteochondral interface. We observed mixed COL2/COL1 tissue in Defect Only group, while both RGD and RGD/RGDW groups showed hyaline cartilage-like COL2 expression only (Fig. 6F). At the osteochondral interface, in Defect Only group, COL1 expression was not limited to the bone tissue, but also detected in the cartilage tissue near the interface (Fig. 6G1). In RGD group, the cartilaginous repair tissue that extends into the subchondral bone showed presence of both hyaline and fibrous markers (Fig. 6G2). In RGD/RGDW group, COL2 expression level diminishes at the interface and transitions into COL 1 expression (Fig. 6G3). COL1 expression was not detected in neocartilage tissue near the osteochondral interface.

Through microCT imaging, we evaluated the degree of subchondral bone regeneration qualitatively and quantitatively. Fig. 7A shows 2D cross-sectional images (Fig. 7A1-7A3) and 3D reconstructed ROI (bottom) of worst (left) and best (right) cases of bone regeneration (Fig. 7A4-7A 6). The extent of bone regeneration was quantified as % BV/TV in Fig. 7B. Bilayered RGD/RGDW exhibited more bone regeneration than RGD with statistical significance (Fig. 7B). Although the average % BV/TV was only marginally higher for RGD/RGDW group (40.2 ± 7.2 %) compared to control (36.9 ± 17.1 %) due to high sample variability, it is important to note that a majority of the animals showed poor bone regeneration (20–25 % BV/TV) (Fig. 7B). Results from the rabbit osteochondral defect model demonstrate that RGD/RGDW bilayer regenerates hyaline-like neotissue that is confined to the articular cartilage. Moreover, hypertrophic RGDW bottom layer promotes osseointegration for integrative defect repair.

4. Discussion

Numerous studies have explored the use of cartilage-bone multilayered or gradient scaffolds with MSCs as cell source for osteochondral defect repair. Inducing MSC chondrogenesis and osteogenesis within the appropriate layers involves a multifaceted interplay of bioactive factors, biomimetic materials and scaffold design [40]. Here, we engineered a hyaline cartilage-hypertrophic cartilage bilayer graft with chondrocytes. The scaffold is conceptually simple and easy to fabricate via cryogelation (Fig. 1A). With RGD-modified CSMA cryogel (RGD group) as the basic framework for both layers, WH is incorporated into the bottom hypertrophic layer (RGDW group) to form RGD/RGDW bilayer scaffold. Since the chondro-conductive nature of RGD cryogel was previously reported [22], this study primarily focuses on the hypertrophic nature of RGDW cryogel.

Bioceramics such as HAp [23–26] and bioactive glass [41,42] have been incorporated in biomaterial scaffolds to induce chondrocyte hypertrophy for osteochondral interface regeneration. Studies have employed MSC-derived chondrocytes [43–45], given their unstable chondrocytic phenotype and tendency toward terminal hypertrophic differentiation. Although regarded as a phenomenon to be avoided in articular cartilage tissue engineering research, chondrocyte hypertrophy is important in the context of osteochondral interface regeneration. To the best of our knowledge, this is the first study that employs WH for chondrocyte hypertrophy induction. We demonstrated that WH induces hypertrophic changes, both *in vitro* and *in vivo*. While normal articular chondrocytes typically display low level of proliferation, hypertrophic chondrocytes are highly proliferative cells [46]. Compared to RGD group, RGDW group showed higher proliferation rate in CCK-8 and PicoGreen dsDNA assays (Fig. 3B–C). WH incorporation in RGDW group promoted hypertrophic gene and protein expressions. Chondrocytes seeded in RGDW group exhibited upregulated hypertrophy-related gene/protein expression and downregulated chondrogenic gene/protein expression, whereas an opposite trend was observed in RGD group (Fig. 2D–I, 4E-F). Chondrocyte-laden RGDW cryogel generated ectopic COLX-high hypertrophic cartilage tissue after 6 weeks of subcutaneous implantation (Fig. 4D). Combined, RGD/RGDW bilayer showed distinctly stratified COL2 and COLX expressions (Fig. 4G), illustrating the capacity to produce hyaline- and hypertrophic-quality cartilage tissue in their respective layers. While chondrocyte hypertrophy is crucial for osteochondral interface regeneration, it is important that WH's influence does not extend to the adjacent hyaline region.

Chondrocyte hypertrophy-inducing effects of Ca^{2+} and PO_4^{3-} ions have been reported previously [35–38]. Mg^{2+} ions also appear to play a role in chondrocyte hypertrophy [30]. Increase in Mg^{2+} ion concentration was generally correlated with an increase in hypertrophy-related gene and protein expression and cell proliferation (Supplementary Fig. 2). However, COLX gene and protein expression diminished in 5 mM Mg^{2+} group. Therefore, it is important to control scaffold design parameter, including WH concentration, to maintain an acceptable dose

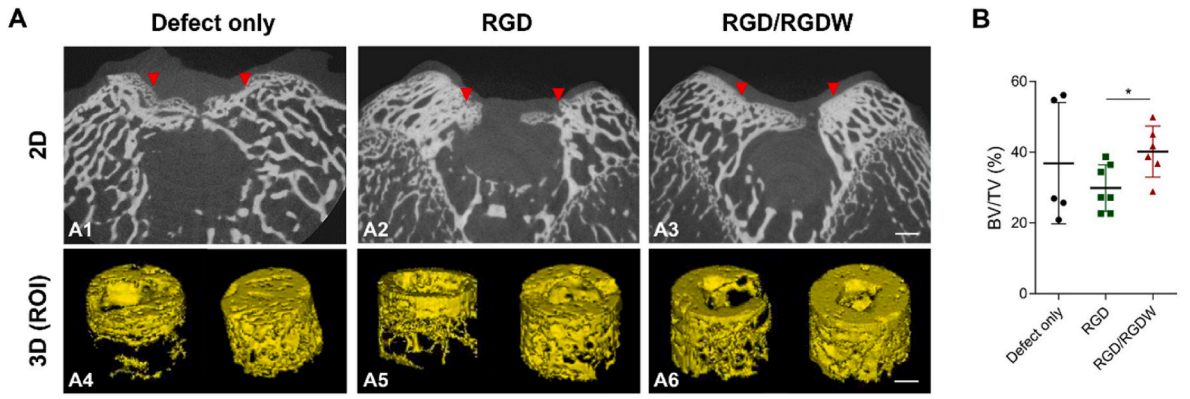

Fig. 7. RGD/RGDW bilayer promotes subchondral bone regeneration. (A) Micro-CT 2D cross-sectional image (A1-A3) and 3D reconstructed image (A4-A6) of ROI (colored in yellow). ROI of worst(left) and best(right) cases of bone regeneration are shown. Scale bar = 1 mm. (B) Percentage of regenerated bone over total volume (% BV/TV), quantified from 3D reconstructed ROI. Error bars indicate SD. *p < 0.05.

of Mg^{2+} ion release for the desired hypertrophic effect. Since cell volume increase accompanies chondrocyte hypertrophy, an ion transporter that modulates extracellular and intracellular ion balance may have played a key role in this ion-driven cell response. Transient receptor potential cation channel subfamily M, member 7 (TRPM7) is a voltage-gated cationic channel that mediates the influx and homeostasis of both Ca^{2+} and Mg^{2+}. TRPM7 channel and its activation have been associated with pre-hypertrophic [47] and hypertrophic [48] gene expression, and hypertrophic cartilage formation and maturation [49,50], potentially through the regulation of PI3K-Akt signaling pathway [51,52]. Intracellular Mg^{2+} has shown to promote osteogenesis via Notch signaling activation [53], a pathway also required for the onset of chondrocyte hypertrophy [54]. The underlying mechanism of Mg^{2+} involvement is still unclear and requires further investigation. Given its well-established role in ATP transport [55] and cell proliferation [56], Mg^{2+} supports the high proliferative activity of hypertrophic chondrocytes. For this study, we chose WH given its unique release of Mg^{2+} ions that amplifies hypertrophic response.

Chondrocyte-laden RGDW cryogel mineralized in *in vivo* bone microenvironment, which is important for calcified cartilage regeneration (Fig. 5). Hypertrophic chondrocytes secrete matrix vesicles containing calcium phosphate crystals, which eventually penetrate the membrane and are released into the extracellular fluid [57,58]. Moreover, COLX secreted by hypertrophic chondrocytes is known to be involved in matrix organization, calcium binding and matrix vesicle compartmentalization [21]. In the right context of physiochemical and biochemical factors, preformed crystals deposit on the surrounding ECM, and serve as nucleation sites for hydroxyapatite crystal growth and propagation. Chondroitin sulfate (CS), a fundamental component of the cryogel backbone, and WH are believed to contribute to biomineralization kinetics and ion recruitment. Due to its negative charge and affinity for cations like Ca^{2+}, CS can 1) promote initial binding of preformed crystals [59] and 2) provide a mineralized surface that is energetically favorable for subsequent crystal formation. Given its release of free Ca^{2+} and PO_4^{3-} ions, WH can serve as an ion reservoir for crystal growth. Therefore, mineralization was mediated by WH-induced hypertrophic chondrocytes and assisted by CS and WH.

After confirming that RGDW group forms calcified cartilage *in vivo*, we hypothesized that RGD/RGDW bilayer graft would be appropriate for osteochondral regeneration. To evaluate the effect of incorporating a bottom hypertrophic layer, rabbit osteochondral defects were implanted with either RGD/RGDW (bilayer) or RGD (monolayer) graft for 12 weeks. The extent and quality of repair was assessed through histological, immunostaining and microCT analyses. Macroscopically, the repaired tissue of Defect only group showed good integration with surrounding native tissue (Fig. 6B), but was not hyaline in quality (Fig. 6C1-6C2, 6E1, 6F1). Repaired tissue of both RGD and RGD/RGDW groups displayed intense red Safranin-O staining (sGAG) and blue MTC staining (collagen) with round cells housed in lacunae, which are characteristics of hyaline cartilage (Fig. 6C3-6C6, 6E2-3). At the cartilage-bone interface, in RGD/RGDW group, COL2 expression level gradually diminishes and transitions into COL1 expression (Fig. 6G3). This collagen expression pattern matches the collagen composition of the osteochondral tissue: articular cartilage (COL2 high)-calcified cartilage (COL2 low)-subchondral bone (COL1 high) [13]. In RGD group, cartilage neotissue penetrated deep into the subchondral bone region and was mixed (hyaline + fibrous) cartilage (Fig. 6G2).

Moreover, RGD group showed signs of vascular infiltration into the hyaline region. Preventing vascular channels from crossing into newly regenerated avascular hyaline cartilage is crucial to avoid ectopic mineralization [60]. RGD/RGDW group showed regenerated hyaline cartilage tissue that is confined to its respective layer via calcified cartilage and tidemark. Correspondingly, ICRS II histological score was ~14 % higher for RGD/RDW group (Fig. 6D). Based on 14 parameters related to chondrocyte phenotype and tissue structure [61], ICRS II scoring system is more comprehensive than other scoring systems (ICRS I [62] and modified O'Driscoll [63]) and thus, appropriate for evaluating the benefits of adapting RGD/RGDW bilayer.

Furthermore, RGD/RGDW group resulted in 10.3 % more subchondral bone regeneration than RGD group (Fig. 7). Although the average % BV/TV was almost on par with that of RGD/RGDW, subchondral bone regeneration of Defect only group exhibited high sample-to-sample variation and wide sample range. The degree of bone regeneration in untreated, empty osteochondral defects is highly contingent upon the individual's inherent self-repair capacity, which can be influenced by multiple factors including age, health condition and stress. The fact that RGD/RGDW group exhibited the highest % BV/TV with low SD suggests that the bottom hypertrophic cartilage layer consistently promoted osseointegration with surrounding bone. In fact, multiple studies have demonstrated that implantation of hypertrophic chondrocyte or cartilage promotes bone regeneration [64,65]. We can turn to the natural bone development and healing process for explanation [49,50]. Hypertrophic chondrocytes secrete vascular endothelial growth factor (VEGF) that recruits blood vessels from adjacent bone tissue. The mineralized cartilage attracts osteoblasts and other cells involved in bone remodeling and regeneration. The mineralized matrix also releases signaling molecules or growth factors that stimulate osteoblasts to deposit new bone tissue in close proximity to the mineralized cartilage. This gradual transition from mineralized cartilage to bone allows for a more seamless integration between tissue engineered cartilage graft and native subchondral bone.

5. Conclusion

In this study, we incorporated WH into a chondro-condutive cryogel to promote chondrocyte hypertrophy. RGDW group exhibited upregulated hypertrophy-related gene expression *in vitro* and accumulation of COLX for ectopic hypertrophic cartilage formation *in vivo*. Subsequently, RGDW cryogel was combined with RGD cryogel into bilayer (RGD/RGDW group) and implanted into rabbit osteochondral defect. The hypertrophic cartilage layer, which mineralized into calcified cartilage, facilitated osseointegration with surrounding bone, which is critical for graft-to-tissue integration. Moreover, RGD/RGDW group regenerated hyaline-like tissue in the articular cartilage layer.

Ethics approval and consent to participate

All animal protocols were in accordance with the Guidelines for Care and Use of Laboratory Animals of Seoul National University (Approval No. SNU-170607-3-7 and SNU-210528-3-2).

CRediT authorship contribution statement

Rachel H. Koh: Writing – review & editing, Writing – original draft, Visualization, Validation, Resources, Project administration, Methodology, Investigation, Funding acquisition, Formal analysis, Data curation, Conceptualization. **Junhee Kim:** Validation, Resources, Project administration, Methodology, Investigation, Formal analysis. **Jeong-Uk Kim:** Resources, Project administration, Methodology, Investigation. **Seunghyun L. Kim:** Methodology, Investigation. **Arun Kumar Rajendran:** Writing – review & editing, Methodology, Investigation, Funding acquisition. **Seunghun S. Lee:** Methodology, Writing – review & editing. **Heesoo Lee:** Investigation. **Joo Hyun Kim:** Methodology, Investigation. **Ji Hoon Jeong:** Methodology, Investigation. **Yongsung Hwang:** Methodology, Investigation. **Jong Woo Bae:** Writing – review & editing, Supervision, Resources, Investigation. **Nathaniel S. Hwang:** Writing – review & editing, Supervision, Funding acquisition, Conceptualization.

Declaration of competing interest

The authors declare that they have no known competing financial interests or personal relationships that could have appeared to influence the work reported in this paper.

Acknowledgements

This work was supported by the National Research Foundation of Korea (NRF) grant funded by the Korean government (NRF-2021K1A3A1A57086407, NRF-2021R1A2C2008821, NRF-2022R1I1A1A01071991). Arun Kumar Rajendran was supported by the National Research Foundation of Korea (NRF) grant Brain Pool program funded by the Ministry of Science and ICT through the National Research Foundation of Korea (2020H1D3A1A04081286). The Institute of Engineering Research at Seoul National University provided research facilities, and additional support came from the SNU Engineering-Medicine Collaboration grant.

Appendix A. Supplementary data

Supplementary data to this article can be found online at https://doi.org/10.1016/j.bioactmat.2024.06.018.

References

[1] H.J. Mankin, The response of articular cartilage to mechanical injury, J Bone Joint Surg Am 64 (3) (1982) 460–466.
[2] R. Cao, A. Zhan, Z. Ci, C. Wang, Y. She, Y. Xu, K. Xiao, H. Xia, L. Shen, D. Meng, C. Chen, A biomimetic biphasic scaffold consisting of decellularized cartilage and decalcified bone matrixes for osteochondral defect repair, Front. Cell Dev. Biol. 9 (2021) 639006, https://doi.org/10.3389/fcell.2021.639006.
[3] T.J. Levingstone, A. Matsiko, G.R. Dickson, F.J. O'Brien, J.P. Gleeson, A biomimetic multi-layered collagen-based scaffold for osteochondral repair, Acta Biomater. 10 (5) (2014) 1996–2004, https://doi.org/10.1016/j.actbio.2014.01.005.
[4] T.J. Levingstone, E. Thompson, A. Matsiko, A. Schepens, J.P. Gleeson, F.J. O'Brien, Multi-layered collagen-based scaffolds for osteochondral defect repair in rabbits, Acta Biomater. 32 (2016) 149–160, https://doi.org/10.1016/j.actbio.2015.12.034.
[5] C. Parisi, L. Salvatore, L. Veschini, M.P. Serra, C. Hobbs, M. Madaghiele, A. Sannino, L. Di Silvio, Biomimetic gradient scaffold of collagen-hydroxyapatite for osteochondral regeneration, J. Tissue Eng. 11 (2020) 2041731419896068, https://doi.org/10.1177/2041731419896068.
[6] J.M. Oliveira, M.T. Rodrigues, S.S. Silva, P.B. Malafaya, M.E. Gomes, C.A. Viegas, I. R. Dias, J.T. Azevedo, J.F. Mano, R.L. Reis, Novel hydroxyapatite/chitosan bilayered scaffold for osteochondral tissue-engineering applications: scaffold design and its performance when seeded with goat bone marrow stromal cells, Biomaterials 27 (36) (2006) 6123–6137, https://doi.org/10.1016/j.biomaterials.2006.07.034.
[7] H. Cai, Y. Yao, Y. Xu, Q. Wang, W. Zou, J. Liang, Y. Sun, C. Zhou, Y. Fan, X. Zhang, A Col I and BCP ceramic bi-layer scaffold implant promotes regeneration in osteochondral defects, RSC Adv. 9 (7) (2019) 3740–3748, https://doi.org/10.1039/c8ra09171d.
[8] J. Jeong, J.H. Kim, J.H. Shim, N.S. Hwang, C.Y. Heo, Bioactive calcium phosphate materials and applications in bone regeneration, Biomater. Res. 23 (2019) 4, https://doi.org/10.1186/s40824-018-0149-3.
[9] C.J. Deng, Q.Q. Yao, C. Feng, J.Y. Li, L.M. Wang, G.F. Cheng, M.C. Shi, L. Chen, J. Chang, C.T. Wu, 3D printing of bilineage constructive biomaterials for bone and cartilage regeneration, Adv. Funct. Mater. 27 (36) (2017). ARTN170311710.1002/adfm.201703117.
[10] C. Qin, J.G. Ma, L. Chen, H.S. Ma, H. Zhuang, M. Zhang, Z.G. Huan, J. Chang, N. Ma, C.T. Wu, 3D bioprinting of multicellular scaffolds for osteochondral regeneration, Mater. Today 49 (2021) 68–84, https://doi.org/10.1016/j.mattod.2021.04.016.
[11] R. Lin, C. Deng, X. Li, Y. Liu, M. Zhang, C. Qin, Q. Yao, L. Wang, C. Wu, Copper-incorporated bioactive glass-ceramics inducing anti-inflammatory phenotype and regeneration of cartilage/bone interface, Theranostics 9 (21) (2019) 6300–6313, https://doi.org/10.7150/thno.36120.
[12] X. Wu, M. Zhou, F. Jiang, S. Yin, S. Lin, G. Yang, Y. Lu, W. Zhang, X. Jiang, Marginal sealing around integral bilayer scaffolds for repairing osteochondral defects based on photocurable silk hydrogels, Bioact. Mater. 6 (11) (2021) 3976–3986, https://doi.org/10.1016/j.bioactmat.2021.04.005.
[13] Y. Zhang, F. Wang, H. Tan, G. Chen, L. Guo, L. Yang, Analysis of the mineral composition of the human calcified cartilage zone, Int. J. Med. Sci. 9 (5) (2012) 353–360, https://doi.org/10.7150/ijms.4276.
[14] T.R. Oegema Jr., R.J. Carpenter, F. Hofmeister, R.C. Thompson Jr., The interaction of the zone of calcified cartilage and subchondral bone in osteoarthritis, Microsc. Res. Tech. 37 (4) (1997) 324–332, https://doi.org/10.1002/(SICI)1097-0029(19970515)37:4<324::AID-JEMT7>3.0.CO;2-332.
[15] I. Redler, V.C. Mow, M.L. Zimny, J. Mansell, The ultrastructure and biomechanical significance of the tidemark of articular cartilage, Clin. Orthop. Relat. Res. 112 (1975) 357–362.
[16] M. Liu, X. Ke, Y. Yao, F. Wu, S. Ye, L. Zhang, G. Yang, M. Shen, Y. Li, X. Yang, C. Zhong, C. Gao, Z. Gou, Artificial osteochondral interface of bioactive fibrous membranes mediating calcified cartilage reconstruction, J. Mater. Chem. B 9 (37) (2021) 7782–7792, https://doi.org/10.1039/d1tb01238j.
[17] M.K. Boushell, C.T. Hung, E.B. Hunziker, E.J. Strauss, H.H. Lu, Current strategies for integrative cartilage repair, Connect. Tissue Res. 58 (5) (2017) 393–406, https://doi.org/10.1080/03008207.2016.1231180.
[18] J. Yang, Y. Liu, L. He, Q. Wang, L. Wang, T. Yuan, Y. Xiao, Y. Fan, X. Zhang, Icariin conjugated hyaluronic acid/collagen hydrogel for osteochondral interface restoration, Acta Biomater. 74 (2018) 156–167, https://doi.org/10.1016/j.actbio.2018.05.005.
[19] X. Yu, T. Zhao, Y. Qi, J. Luo, J. Fang, X. Yang, X. Liu, T. Xu, Q. Yang, Z. Gou, X. Dai, In vitro chondrocyte responses in Mg-doped wollastonite/hydrogel composite scaffolds for osteochondral interface regeneration, Sci. Rep. 8 (1) (2018) 17911, https://doi.org/10.1038/s41598-018-36200-x.
[20] M.K. Boushell, N.T. Khanarian, R.Z. LeGeros, H.H. Lu, Effect of ceramic calcium-phosphorus ratio on chondrocyte-mediated biosynthesis and mineralization, J. Biomed. Mater. Res. 105 (10) (2017) 2694–2702, https://doi.org/10.1002/jbm.a.36122.
[21] C.A. Knuth, E. Andres Sastre, N.B. Fahy, J. Witte-Bouma, Y. Ridwan, E. M. Strabbing, M.J. Koudstaal, J. van de Peppel, E.B. Wolvius, R. Narcisi, E. Farrell, Collagen type X is essential for successful mesenchymal stem cell-mediated cartilage formation and subsequent endochondral ossification, Eur. Cell. Mater. 38 (2019) 106–122, https://doi.org/10.22203/eCM.v038a09.
[22] R.H. Koh, J. Kim, S.H.L. Kim, N.S. Hwang, RGD-incorporated biomimetic cryogels for hyaline cartilage regeneration, Biomed. Mater. 17 (2) (2022), https://doi.org/10.1088/1748-605X/ac51b7.
[23] N.T. Khanarian, N.M. Haney, R.A. Burga, H.H. Lu, A functional agarose-hydroxyapatite scaffold for osteochondral interface regeneration, Biomaterials 33 (21) (2012) 5247–5258, https://doi.org/10.1016/j.biomaterials.2012.03.076.
[24] S. Korpayev, O. Toprak, G. Kaygusuz, M. Sen, K. Orhan, A. Karakecili, Regulation of chondrocyte hypertrophy in an osteochondral interface mimicking gel matrix, Colloids Surf. B Biointerfaces 193 (2020) 111111, https://doi.org/10.1016/j.colsurfb.2020.111111.

[25] F. You, X. Chen, D.M.L. Cooper, T. Chang, B.F. Eames, Homogeneous hydroxyapatite/alginate composite hydrogel promotes calcified cartilage matrix deposition with potential for three-dimensional bioprinting, Biofabrication 11 (1) (2018) 015015, https://doi.org/10.1088/1758-5090/aaf44a.
[26] A. Sadeghianmaryan, S. Naghieh, Z. Yazdanpanah, H. Alizadeh Sardroud, N. K. Sharma, L.D. Wilson, X. Chen, Fabrication of chitosan/alginate/hydroxyapatite hybrid scaffolds using 3D printing and impregnating techniques for potential cartilage regeneration, Int. J. Biol. Macromol. 204 (2022) 62–75, https://doi.org/10.1016/j.ijbiomac.2022.01.201.
[27] H.D. Kim, H.L. Jang, H.Y. Ahn, H.K. Lee, J. Park, E.S. Lee, E.A. Lee, Y.H. Jeong, D. G. Kim, K.T. Nam, N.S. Hwang, Biomimetic whitlockite inorganic nanoparticles-mediated in situ remodeling and rapid bone regeneration, Biomaterials 112 (2017) 31–43, https://doi.org/10.1016/j.biomaterials.2016.10.009.
[28] T. Hu, H. Xu, C. Wang, H. Qin, Z. An, Magnesium enhances the chondrogenic differentiation of mesenchymal stem cells by inhibiting activated macrophage-induced inflammation, Sci. Rep. 8 (1) (2018) 3406, https://doi.org/10.1038/s41598-018-21783-2.
[29] Y. Zhang, J. Xu, Y.C. Ruan, M.K. Yu, M. O'Laughlin, H. Wise, D. Chen, L. Tian, D. Shi, J. Wang, S. Chen, J.Q. Feng, D.H. Chow, X. Xie, L. Zheng, L. Huang, S. Huang, K. Leung, N. Lu, L. Zhao, H. Li, D. Zhao, X. Guo, K. Chan, F. Witte, H. C. Chan, Y. Zheng, L. Qin, Implant-derived magnesium induces local neuronal production of CGRP to improve bone-fracture healing in rats, Nat. Med. 22 (10) (2016) 1160–1169, https://doi.org/10.1038/nm.4162.
[30] Y. Dou, N. Li, Y. Zheng, Z. Ge, Effects of fluctuant magnesium concentration on phenotype of the primary chondrocytes, J. Biomed. Mater. Res. 102 (12) (2014) 4455–4463, https://doi.org/10.1002/jbm.a.35113.
[31] A. Trengove, C. Di Bella, A.J. O'Connor, The challenge of cartilage integration: understanding a major barrier to chondral repair, Tissue Eng., Part B 28 (1) (2022) 114–128, https://doi.org/10.1089/ten.TEB.2020.0244.
[32] H.D. Kim, J. Heo, Y. Hwang, S.Y. Kwak, O.K. Park, H. Kim, S. Varghese, N. S. Hwang, Extracellular-matrix-based and Arg-Gly-Asp-modified photopolymerizing hydrogels for cartilage tissue engineering, Tissue Eng. 21 (3–4) (2015) 757–766, https://doi.org/10.1089/ten.TEA.2014.0233.
[33] M. Bruderer, R.G. Richards, M. Alini, M.J. Stoddart, Role and regulation of RUNX2 in osteogenesis, Eur. Cell. Mater. 28 (2014) 269–286, https://doi.org/10.22203/ecm.v028a19.
[34] H. Akiyama, M.C. Chaboissier, J.F. Martin, A. Schedl, B. de Crombrugghe, The transcription factor Sox9 has essential roles in successive steps of the chondrocyte differentiation pathway and is required for expression of Sox5 and Sox6, J. Bone Miner. Res. 17 (2002). S142-S142.
[35] Y.K. Jung, M.S. Han, H.R. Park, E.J. Lee, J.A. Jang, G.W. Kim, S.Y. Lee, D. Moon, S. Han, Calcium-phosphate complex increased during subchondral bone remodeling affects earlystage osteoarthritis, Sci. Rep. 8 (1) (2018) 487, https://doi.org/10.1038/s41598-017-18946-y.
[36] D. Wang, L. Canaff, D. Davidson, A. Corluka, H. Liu, G.N. Hendy, J.E. Henderson, Alterations in the sensing and transport of phosphate and calcium by differentiating chondrocytes, J. Biol. Chem. 276 (36) (2001) 33995–34005, https://doi.org/10.1074/jbc.M007757200.
[37] R. Kandel, M. Hurtig, M. Grynpas, Characterization of the mineral in calcified articular cartilagenous tissue formed in vitro, Tissue Eng. 5 (1) (1999) 25–34, https://doi.org/10.1089/ten.1999.5.25.
[38] L.N. Wu, Y. Ishikawa, G.R. Sauer, B.R. Genge, F. Mwale, H. Mishima, R.E. Wuthier, Morphological and biochemical characterization of mineralizing primary cultures of avian growth plate chondrocytes: evidence for cellular processing of Ca2+ and Pi prior to matrix mineralization, J. Cell. Biochem. 57 (2) (1995) 218–237, https://doi.org/10.1002/jcb.240570206.
[39] S. Kauppinen, S.S. Karhula, J. Thevenot, T. Ylitalo, L. Rieppo, I. Kestila, M. Haapea, I. Hadjab, M.A. Finnila, E. Quenneville, M. Garon, H.K. Gahunia, K.P.H. Pritzker, M.D. Buschmann, S. Saarakkala, H.J. Nieminen, 3D morphometric analysis of calcified cartilage properties using micro-computed tomography, Osteoarthritis Cartilage 27 (1) (2019) 172–180, https://doi.org/10.1016/j.joca.2018.09.009.
[40] C. Deng, J. Chang, C. Wu, Bioactive scaffolds for osteochondral regeneration, J Orthop Translat 17 (2019) 15–25, https://doi.org/10.1016/j.jot.2018.11.006.
[41] J. Jiang, A. Tang, G.A. Ateshian, X.E. Guo, C.T. Hung, H.H. Lu, Bioactive stratified polymer ceramic-hydrogel scaffold for integrative osteochondral repair, Ann. Biomed. Eng. 38 (6) (2010) 2183–2196, https://doi.org/10.1007/s10439-010-0038-y.
[42] N. Mohan, J. Wilson, D. Joseph, D. Vaikkath, P.D. Nair, Biomimetic fiber assembled gradient hydrogel to engineer glycosaminoglycan enriched and mineralized cartilage: an in vitro study, J. Biomed. Mater. Res. 103 (12) (2015) 3896–3906, https://doi.org/10.1002/jbm.a.35506.
[43] Y. Wang, S.H. Wu, M.A. Kuss, P.N. Streube, B. Duan, Effects of hydroxyapatite and hypoxia on chondrogenesis and hypertrophy in 3D bioprinted ADMSC laden constructs, ACS Biomater. Sci. Eng. 3 (5) (2017) 826–835, https://doi.org/10.1021/acsbiomaterials.7b00101.
[44] A. Kosik-Koziol, M. Costantini, A. Mroz, J. Idaszek, M. Heljak, J. Jaroszewicz, E. Kijenska, K. Szoke, N. Frerker, A. Barbetta, J.E. Brinchmann, W. Swieszkowski, 3D bioprinted hydrogel model incorporating beta-tricalcium phosphate for calcified cartilage tissue engineering, Biofabrication 11 (3) (2019) 035016, https://doi.org/10.1088/1758-5090/ab15cb.
[45] W.D. Lee, M.B. Hurtig, R.M. Pilliar, W.L. Stanford, R.A. Kandel, Engineering of hyaline cartilage with a calcified zone using bone marrow stromal cells, Osteoarthritis Cartilage 23 (8) (2015) 1307–1315, https://doi.org/10.1016/j.joca.2015.04.010.
[46] V.R. Preedy, V.B. Patel, Aging : Oxidative Stress and Dietary Antioxidants, second ed., Academic Press, an imprint of Elsevier, London, United Kingdom ; San Diego, CA, United States, 2020.
[47] G. Ma, Y. Yang, Y. Chen, X. Wei, J. Ding, R.P. Zhou, W. Hu, Blockade of TRPM7 alleviates chondrocyte apoptosis and articular cartilage damage in the adjuvant arthritis rat model through regulation of the Indian hedgehog signaling pathway, Front. Pharmacol. 12 (2021) 655551, https://doi.org/10.3389/fphar.2021.655551.
[48] D. Lu, J. Qu, L. Sun, Q. Li, H. Ling, N. Yang, T. Ma, Q. Wang, M. Li, K. Zhang, Z. Li, Ca2+/Mg2+ homeostasisrelated TRPM7 channel mediates chondrocyte hypertrophy via regulation of the PI3KAkt signaling pathway, Mol. Med. Rep. 16 (4) (2017) 5699–5705, https://doi.org/10.3892/mmr.2017.7300.
[49] N. Qian, A. Ichimura, D. Takei, R. Sakaguchi, A. Kitani, R. Nagaoka, M. Tomizawa, Y. Miyazaki, H. Miyachi, T. Numata, S. Kakizawa, M. Nishi, Y. Mori, H. Takeshima, TRPM7 channels mediate spontaneous Ca(2+) fluctuations in growth plate chondrocytes that promote bone development, Sci. Signal. 12 (576) (2019), https://doi.org/10.1126/scisignal.aaw4847.
[50] M. Shin, S. Mori, T. Mizoguchi, A. Arai, H. Kajiya, F. Okamoto, J.D. Bartlett, M. Matsushita, N. Udagawa, K. Okabe, Mesenchymal cell TRPM7 expression is required for bone formation via the regulation of chondrogenesis, Bone 166 (2023) 116579, https://doi.org/10.1016/j.bone.2022.116579.
[51] X. Zhang, H. Zu, D. Zhao, K. Yang, S. Tian, X. Yu, F. Lu, B. Liu, X. Yu, B. Wang, W. Wang, S. Huang, Y. Wang, Z. Wang, Z. Zhang, Ion channel functional protein kinase TRPM7 regulates Mg ions to promote the osteoinduction of human osteoblast via PI3K pathway: in vitro simulation of the bone-repairing effect of Mg-based alloy implant, Acta Biomater. 63 (2017) 369–382, https://doi.org/10.1016/j.actbio.2017.08.051.
[52] J. Chen, R. Crawford, Y. Xiao, Vertical inhibition of the PI3K/Akt/mTOR pathway for the treatment of osteoarthritis, J. Cell. Biochem. 114 (2) (2013) 245–249, https://doi.org/10.1002/jcb.24362.
[53] J.M. Diaz-Tocados, C. Herencia, J.M. Martinez-Moreno, A. Montes de Oca, M. E. Rodriguez-Ortiz, N. Vergara, A. Blanco, S. Steppan, Y. Almaden, M. Rodriguez, J. R. Munoz-Castaneda, Magnesium chloride promotes osteogenesis through Notch signaling activation and expansion of mesenchymal stem cells, Sci. Rep. 7 (1) (2017) 7839, https://doi.org/10.1038/s41598-017-08379-y.
[54] Y. Hosaka, T. Saito, S. Sugita, T. Hikata, H. Kobayashi, A. Fukai, Y. Taniguchi, M. Hirata, H. Akiyama, U.I. Chung, H. Kawaguchi, Notch signaling in chondrocytes modulates endochondral ossification and osteoarthritis development, Proc. Natl. Acad. Sci. U. S. A 110 (5) (2013) 1875–1880, https://doi.org/10.1073/pnas.1207458110.
[55] M.J. Nadler, M.C. Hermosura, K. Inabe, A.L. Perraud, Q. Zhu, A.J. Stokes, T. Kurosaki, J.P. Kinet, R. Penner, A.M. Scharenberg, A. Fleig, LTRPC7 is a Mg. ATP-regulated divalent cation channel required for cell viability, Nature 411 (6837) (2001) 590–595, https://doi.org/10.1038/35079092.
[56] L.V. Ryazanova, L.J. Rondon, S. Zierler, Z. Hu, J. Galli, T.P. Yamaguchi, A. Mazur, A. Fleig, A.G. Ryazanov, TRPM7 is essential for Mg(2+) homeostasis in mammals, Nat. Commun. 1 (2010) 109, https://doi.org/10.1038/ncomms1108.
[57] A.L. Boskey, Pathogenesis of cartilage calcification: mechanisms of crystal deposition in cartilage, Curr. Rheumatol. Rep. 4 (3) (2002) 245–251, https://doi.org/10.1007/s11926-002-0072-3.
[58] T. Hasegawa, H. Hongo, T. Yamamoto, M. Abe, H. Yoshino, M. Haraguchi-Kitakamae, H. Ishizu, T. Shimizu, N. Iwasaki, N. Amizuka, Matrix vesicle-mediated mineralization and osteocytic regulation of bone mineralization, Int. J. Mol. Sci. 23 (17) (2022), https://doi.org/10.3390/ijms23179941.
[59] H.D. Kim, E.A. Lee, Y.H. An, S.L. Kim, S.S. Lee, S.J. Yu, H.L. Jang, K.T. Nam, S. G. Im, N.S. Hwang, Chondroitin sulfate-based biomineralizing surface hydrogels for bone tissue engineering, ACS Appl. Mater. Interfaces 9 (26) (2017) 21639–21650, https://doi.org/10.1021/acsami.7b04114.
[60] E.B. Hunziker, I.M. Driesang, C. Saager, Structural barrier principle for growth factor-based articular cartilage repair, Clin. Orthop. Relat. Res. 391 (Suppl) (2001) S182–S189, https://doi.org/10.1097/00003086-200110001-00018.
[61] P. Mainil-Varlet, B. Van Damme, D. Nesic, G. Knutsen, R. Kandel, S. Roberts, A new histology scoring system for the assessment of the quality of human cartilage repair: ICRS II, Am. J. Sports Med. 38 (5) (2010) 880–890, https://doi.org/10.1177/0363546509359068.
[62] D. Murata, Y. Kunitomi, K. Harada, S. Tokunaga, S. Takao, K. Nakayama, Osteochondral regeneration using scaffold-free constructs of adipose tissue-derived mesenchymal stem cells made by a bio three-dimensional printer with a needle-array in rabbits, Regen Ther 15 (2020) 77–89, https://doi.org/10.1016/j.reth.2020.05.004.
[63] T. Xu, X. Yu, Q. Yang, X. Liu, J. Fang, X. Dai, Autologous micro-fragmented adipose tissue as stem cell-based natural scaffold for cartilage defect repair, Cell Transplant. 28 (12) (2019) 1709–1720, https://doi.org/10.1177/0963689719880527.
[64] I. Carmon, A. Zobrab, M. Alterman, R. Tabib, A. Cohen, L. Kandel, A. Greenberg, E. Reich, N. Casap, M. Dvir-Ginzberg, Chondrocytes supplemented to bone graft-containing scaffolds expedite cranial defect repair, Sci. Rep. 13 (1) (2023) 19192, https://doi.org/10.1038/s41598-023-46604-z.
[65] K. Bardsley, A. Kwarciak, C. Freeman, I. Brook, P. Hatton, A. Crawford, Repair of bone defects in vivo using tissue engineered hypertrophic cartilage grafts produced from nasal chondrocytes, Biomaterials 112 (2017) 313–323, https://doi.org/10.1016/j.biomaterials.2016.10.014.